Computational and Structural Biotechnology Journal 19 (2021) 897–909

COMPUTATIONAL AND STRUCTURAL BIOTECHNOLOGY JOURNAL

journal homepage: www.elsevier.com/locate/csbj

Molecular basis of ice-binding and cryopreservation activities of type III antifreeze proteins

Seo-Ree Choi [a,1], Jaewang Lee [b,c,1], Yeo-Jin Seo [a,1], Hyun Sun Kong [b], Minjae Kim [d], EonSeon Jin [d], Jung Ryeol Lee [b,e,*], Joon-Hwa Lee [a,*]

[a] Department of Chemistry and Research Institute of Natural Science, Gyeongsang National University, Gyeongnam 52828, Republic of Korea
[b] Department of Obstetrics and Gynecology, Seoul National University Bundang Hospital, Gyeonggi 13620, Republic of Korea
[c] Department of Biomedical Laboratory Science, Eulji University, Gyeonggi 13135, Republic of Korea
[d] Department of Life Science, Hanyang University, Seoul 04763, Republic of Korea
[e] Department of Obstetrics and Gynecology, Seoul National University College of Medicine, Seoul 03080, Republic of Korea

ARTICLE INFO

Article history:
Received 2 October 2020
Received in revised form 13 January 2021
Accepted 14 January 2021
Available online 19 January 2021

Keywords:
Antifreeze protein
Cryopreservation
Ice crystallization inhibition
NMR
Thermal hysteresis

ABSTRACT

Antifreeze proteins (AFPs) can inhibit the freezing of body fluid at subzero temperatures to promote the survival of various organisms living in polar regions. Type III AFPs are categorized into three subgroups, QAE1, QAE2, and SP isoforms, based on differences in their isoelectric points. We determined the thermal hysteresis (TH), ice recrystallization inhibition (IRI), and cryopreservation activity of three isoforms of the notched-fin eelpout AFP and their mutant constructs and characterized their structural and dynamic features using NMR. The QAE1 isoform is the most active among the three classes of III AFP isoforms, and the mutants of inactive QAE2 and SP isoforms, $QAE2^{ACT}$ and SP^{ACT}, displayed the full TH and IRI activities with resepect to QAE1 isoform. Cryopreservation studies using mouse ovarian tissue revealed that the QAE1 isoform and the active mutants, $QAE2^{ACT}$ and SP^{ACT}, more effectively preserved intact follicle morphology and prevented DNA double-strand break damage more efficiently than the inactive isoforms. It was also found that all active AFPs, QAE1, $QAE2^{ACT}$, and SP^{ACT}, formed unique H-bonds with the first 3_{10} helix, an interaction that plays an important role in the formation of anchored clathrate water networks for efficient binding to the primary prism and pyramidal planes of ice crystals, which was disrupted in the inactive isoforms. Our studies provide valuable insights into the molecular mechanism of the TH and IRI activity, as well as the cryopreservation efficiency, of type III AFPs.

1. Introduction

Antifreeze protein (AFP) was first isolated from an Antarctic fish in 1969 [1] and since then has been found in various organisms living in polar regions including fish, insects, plants, bacteria, and fungi [2–6]. The primary indicator for the antifreeze activities of AFPs is thermal hysteresis (TH), which gives rise to a difference between the freezing point (T_f) and melting point (T_m) [2–7]. The mechanism of AFP's TH activity involves binding to ice crystals and inhibiting their growth, and thus AFP is called an ice-binding protein (IBP); such activity results in ice recrystallization inhibition (IRI) [8]. Ice recrystallization produces large ice crystals by growth of small ice crystals, and this is fatal to cells. However, AFPs prevent the recrystallization process through IRI activity, resulting in a cryoprotective effect especially from cell membrane damages [9–11].

Despite the beneficial effects of TH activity, most studies about AFPs have focused on the basic principles of the TH activity rather than its biological applications. Moreover, only a few studies have been conducted on the role of AFPs in cryopreservation of red blood cells, oocytes, embryos, and ovaries [11–14]. Preservation of fertility after cancer treatment has become an important health

Abbreviations: AFP, Antifreeze protein; TH, thermal hysteresis; IBP, ice-binding protein; IRI, ice recrystallization inhibition; OT, ovarian tissue; QAE, quaternary-amino-ethyl; SP, sulfopropyl; IBS, ice-binding surface; H-bond, hydrogen bond; wt, wild-type; nfeAFP, notched-fin eelpout AFP; DSB, double-strand break; TUNEL, terminal deoxynucleotidyl transferase dUTP nick end labelling; EG, ethylene glycol; DMSO, dimethyl sulfoxide; D-PBS, Dulbecco's phosphate-buffered saline; RT, room temperature; CPA, cryoprotective agent.

* Corresponding authors at: Department of Obstetrics and Gynecology, Seoul National University College of Medicine, Seoul 03080, Republic of Korea (J.R. Lee), Department of Chemistry and RINS, Gyeongsang National University, Gyeongnam 52828, Republic of Korea (J.-H. Lee).

E-mail addresses: leejrmd@snu.ac.kr (J.R. Lee), joonhwa@gnu.ac.kr (J.-H. Lee).

[1] These authors contributed equally to this work.

https://doi.org/10.1016/j.csbj.2021.01.016

care issue as survival rates after cancer treatment have increased. Oocyte, embryo, and ovarian tissue (OT) cryopreservation are clinically available options, but improvement of the survival and function of cryopreserved cells and tissue is still necessary. Three previous studies reported beneficial effects of AFPs on ovarian tissue quality after the vitrification-warming process in mouse models [13–15]. However, the exact mechanism and molecular basis of the protective effects have not been fully investigated.

Ovarian tissue cryopreservation has been widely used to preserve fertility in women. It can be applied by either slow freezing or vitrification. In the slow freezing, tissue is slowly frozen to approximately −80 °C, followed by the storage of the tissue in liquid nitrogen at −196 °C [16–18]. Slow freezing shows a limitation which has potential risk for ice crystal formation in the ovarian tissue that may occur mechanical damage to the cells. On the other hand, vitrification is an instant solidification of the solution as a result of increased viscosity during cooling with higher concentrations of cryoprotectants compared with that of used in slow freezing. Notably, vitrification does not make an ice crystal theoretically. Many studies have demonstrated that vitrification is a useful option to cryopreserve ovarian tissue in mouse, sheep, human and others [19–21].

Fish AFPs are grouped into four types on the basis of their structures: alanine-rich α-helical type I AFPs, cysteine-rich type II AFPs, ~7-kDa globular type III AFPs, and glutamate/glutamine-rich α-helical type IV AFPs [2–6]. Type III AFPs are compact globular proteins [22] and have been categorized into two subgroups quaternary-amino-ethyl (QAE), further divided into QAE1 and QAE2 subgroups, and sulfopropyl (SP) sephadex-binding isoforms based on differences in their isoelectric points (Fig. 1) [23,24]. The QAE1 isoform has a much higher TH activity than QAE2 and SP isoforms and can stop ice crystal growth at temperatures below the T_f of the solution [24]. The ice-binding surface (IBS) of a type III AFP (residues 9 – 21 and 41–44 in Fig. 1A) consists of two adjacent surfaces, which bind to the pyramidal and primary prism planes of the ice crystal, respectively (Fig. 1B) [25]. The QAE2 isoform from *Zoarces elongatus Kner* could be converted into active mutants ($QAE2^{ACT}$) obtained by changing of the IBS with the corresponding residues of QAE1, which exhibits TH and IRI effects similar to those of its paralogue QAE1 [25,26]. The $QAE2^{ACT}$ mutants, which bear the substitutions V9Q/V19L/G20V or V9Q/V19L/G20V/I42V, was structurally compared with QAE1 and QAE2 [25]. Vice versa, the inactive mutants of the QAE1 isoform ($QAE1^{INACT}$), which bears the substitutions V20G, L19V/V20G, or Q9V/L19V/V20G, had no TH activity [27]. The active QAE1 isoform and $QAE2^{ACT}$ mutant showed unusual intermolecular hydrogen bonding (H-bonding) interactions between the T18 side-chain and the surface water molecule, whereas this interaction was not observed in the inactive QAE2 isoform and $QAE1^{INACT}$ mutants [26,27]. It has been suggested the anchored clathrate water (ACW) mechanism in which the AFP exhibited H-bonding interactions with an array of surface waters that three-dimensionally match to both the pyramidal and primary prism planes of the ice crystal [28]. Recently, Mahatabuddin *et al.* reported that in type III AFP, the two ice-like water clusters also exhibited a space-match to the primary prism and pyramidal ice planes like ACW [29]. In the ACW mechanism, the AFP-water interaction can be assisted by the hydrophobic interaction via side-chain groups of IBS, which might regulate the TH and IRI activities of AFPs [28,29]. However, the detailed molecular mechanism by which AFPs exhibit cryopreservation effects through TH and/or IRI activities is not well understood and requires not only further biophysical characterization but also further studies of its biological applications.

NMR is a powerful technique for the study of structure, dynamics, and folding of biomolecules such as nucleic acids [30] and proteins [31]. Hydrogen exchange measurement using NMR provides residue-specific information on the thermodynamics and kinetics of H-bonded secondary structure and exposure to solvent water. NOE cross-peaks of the exchangeable protons with water resonance can be used to determine their chemical exchange with solvent water on the s – ms timescale. Recently, in AFPs, NOE data of the amide protons suggested the existence of unusual intermolecular H-bonding interactions between the AFPs and the surface water molecule [26,27].

To understand the molecular basis of the physical and biological function of type III AFPs, we have compared three wild-type (wt) AFPIII isoforms from *Zoarces elongatus Kner* (notched-fin eelpout) (nfeAFP) with their mutants bearing triple mutations of IBS resi-

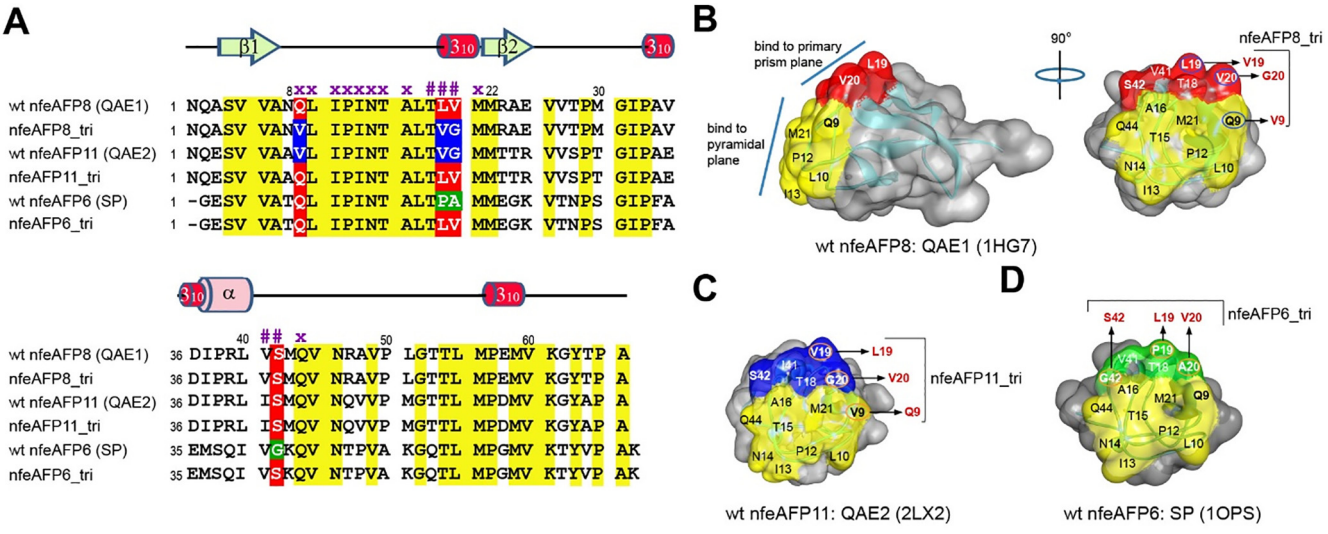

Fig. 1. Sequence homology and IBS of Type III AFPs. (A) Multiple sequence alignment of the type III AFPs. Wt nfeAFP6, wt nfeAFP8, and wt nfeAFP11 are the isoforms 6, 8, and 11 of the notched-fin eelpout type III AFP, respectively. Yellow bars indicate invariant or nearly invariant residues in the type III AFP family. Red, blue, and green bars indicate variant residues in the IBS of type III AFPs. The x and # symbols represent residues composing the pyramidal and primary prism plane-binding surfaces, respectively. IBS of (B) the QAE1 isoform, (HPLC12, PDB id: 1HG7) [22] (C) QAE2 isoform (AFP11, PDB id: 2LX2) [26] and (D) SP isoform (HPLC6, PDB id: 1OPS) [61] of type III AFPs. The surfaces binding to the pyramidal plane of ice are colored yellow and the surfaces binding to the primary prism plane of ice are colored red, blue, or green. (For interpretation of the references to color in this figure legend, the reader is referred to the web version of this article.)

Table 1
Protein information of AFPs studied here.

AFPs	Isoform (pI)	Genbank ID	Origin	Peptide / mutation	Tag
nfeAFP8	QAE1 (9.97)	AB188396.1	*Zoarces elongatus Kner* (Notched-fin eelpout)	N1 – A66 [a] (66 aa)	N-terminal His-tag
nfeAFP8_tri	$QAE1^{INACT}$ (9.97)			Q9V/L19V/V20G	N-terminal His-tag
nfeAFP11	QAE2 (9.70)	AB188399.1	*Zoarces elongatus Kner* (Notched-fin eelpout)	N1 – A66 [a] (66 aa)	N-terminal His-tag
nfeAFP11_tri	$QAE2^{ACT}$ (9.70)			V9Q/V19L/G20V	N-terminal His-tag
nfeAFP6	SP (7.06)	AB188394.1	*Zoarces elongatus Kner* (Notched-fin eelpout)	G2 – K67 [a] (66 aa)	N-terminal His-tag
nfeAFP6_tri	SP^{ACT} (7.06)			P19L/A20V/G42S	N-terminal His-tag

[a] Original residue number; nfeAFP8, N23 – A88; nfeAFP11 N23 – A88; nfeAFP6, G23 – K88.

dues (Fig. 1 and Table 1). For all nfeAFP variants we have determined TH and IRI activities and the cryopreservation effects on mouse OT. The direct comparison of active and inactive variants as for their structural and dynamical properties studied by NMR provide valuable insights into the molecular mechanisms of the TH and IRI activity as well as cryopreservation efficiency of type III AFPs.

2. Materials and methods

2.1. Sample preparation

The DNA coding sequences for the wt nfeAFP8 (aa 1 – 66), wt nfeAFP11 (aa 1 – 66), and wt nfeAFP6 (aa 2 – 67) and their mutants (nfeAFP8_tri, nfeAFP11_tri, and nfeAFP6_tri) (*see* Table 1) were purchased from BIONEER Inc. (Daejeon, Korea) and cloned into *E. coli* expression vector pET28a, which has an N-terminal His-tag. To produce uniformly ^{15}N-labeled or ^{13}C, ^{15}N-labeled wt and mutant nfeAFPs, BL21(DE3) cells were grown in M9 minimal medium that contained 1 g/L $^{15}NH_4Cl$ and/or 2 g/L ^{13}C-glucose as the sole nitrogen and carbon sources. The expressed proteins were purified by Ni–NTA affinity, followed by Sephacryl S-100 gel filtration chromatography (GE Healthcare, Chicago, IL, USA) on a GE AKTA FPLC. The concentrations of all proteins were measured using a Pierce BCA Protein Assay Kit (Thermo Fisher, Scientific, Waltham, MA, USA). For the functional assays, the purified proteins were dissolved in a buffer containing 10 mM sodium phosphate (pH 6.0) and 100 mM NaCl.

2.2. TH measurements

Details of TH measurements have been described in a previous report [27]. The TH of the wt and mutant nfeAFPs was measured using a nanoliter osmometer (Otago, Dunedin, New Zealand). The nfeAFPs were concentrated to 2 mM and then serially diluted to a range of 0.5 ~ 2.0 mM. The TH measurements were repeated at least three times. The protein samples were frozen at −20 °C for 5 min on the center of a freezing stage attached to the stage of a conventional microscope. The frozen protein samples were slowly warmed at a rate of 5 °C/min to be thawed until only a single ice crystal was present. Thereafter, the temperature was lowered at a rate of 0.01 °C/min to observe ice crystal growth. The TH activity was further assayed by observing the morphology of ice crystals, as described in previous reports [32–34]. In this assay, ice crystal nuclei are let to grow in a solution of the protein to be analysed. The formation of spherically shaped crystals indicates the absence of TH activity, while hexagonal bipyramidal-shaped ice crystals indicate the presence of TH activity.

2.3. IRI measurements

The IRI of the wt and mutant nfeAFPs was measured using the protocol, which is reported by Knight *et al.* [35,36] with a slight modification. Purified protein solutions were standardized (with respect to solute concentration) by adding 50 μL of 60% sucrose to 50 μL purified protein. The resulting solution (final concentration: 10 mg/ml) was placed between two circular 12 mm diameter, coverslips, which were gently blotted dry to remove any excess fluid on the surface. The coverslips were placed on the center of a temperature-controlled freezing stage of a nanoliter osmometer (Otago, New Zealand) attached to the stage of a conventional microscope (Zeiss Axiolab, Germany), and then were flash-frozen at −30 °C for 5 min. After complete freezing, the temperature was increased up to −6 °C and held for 30 min and 240 min to allow recrystallization. The coverslips were viewed on the stage using an attached microscope (×100).

2.4. Experimental animals and ethics statement

Five-week-old B6D2F1 female mice (Orient Co., Seongnam, South Korea) were housed under a 12-h light/dark cycle at 22 °C and fed *ad libitum*. Retrieved OTs from the mice (n = 139) were randomly allocated into a sham control (vitrification and warming of OTs without any AFPs) and six experimental groups (wt AFPs nfeAFP6, nfeAFP8, nfeAFP11; mutant forms nfeAFP6_tri, nfeAFP8_tri, and nfeAFP11_tri). All experimental procedures were performed under the approval of the Institutional Animal Care and Use Committee of Seoul National University Bundang Hospital (Approval no.: BA1707-227/062-01).

2.5. Vitrification and warming of mouse ovarian tissue

In accordance with the optimal mouse OT vitrification protocol, vitrification was performed by two-step procedures as previously described [14,37–40]. For the first step, OTs were placed in an equilibration solution consisting of 7.5% (v/v) ethylene glycol (EG; Sigma-Aldrich, St. Louis, MO, USA) and 7.5% (v/v) dimethyl sulfoxide (DMSO; Sigma-Aldrich) in Dulbecco's phosphate-buffered saline (D-PBS, WelGene, Daegu, Korea) with 20% fetal bovine serum (FBS, Gibco, Carlsbad, CA, USA) for 10 min at room temperature (RT). In the second step, equilibrated OTs were moved to the vitrification solution containing 20% EG, 20% DMSO, and 0.5 M sucrose (Sigma-Aldrich) in D-PBS with 20% FBS and placed for 5 min at room temperature. To improve heat conductivity, the OTs were loaded onto an electron microscopic copper grid and the residual solution was removed as previously described [38,41]. Then the OTs were put into 1.8 mL cryovials (Nunc, Roskilde, Denmark) and directly plunged into liquid nitrogen. The OTs were cryopreserved for more than one day. To warm the OTs, tissues were immersed into four steps of serially diluted sucrose media (1.0 M, 0.5 M, 0.25 M, and 0 M sucrose in D-PBS with 20% FBS) in a step-wise manner at RT for 5 min. For each experimental group, 10 mg/mL of the selected nfeAFP was added to the vitrification solution (2nd step of vitrification) and the first step of the warming solution (1 M sucrose solution) as previously described [14].

2.6. Ovarian follicle classification and morphological analysis

All OTs were fixed with Bouin's solution (Sigma-Aldrich) for more than one day, and the OTs of each group were embedded into paraffin blocks. The blocks were serially sectioned at 5-μm thickness. For hematoxylin and eosin (Merck, Darmstadt, Germany) staining, sections at 100-μm intervals were stained and used for ovarian follicle classification/grading and apoptosis detection as described in previous studies [16,42].

The developmental stages of ovarian follicles were classified as follows: 1) primordial, a single layer of flattened pre-granulosa cells; 2) primary, a single layer of granulosa cells, one or more of which is cuboidal; 3) secondary, two or more layers of cuboidal granulosa cells, without the antrum; or 4) antral, multiple layers of cuboidal granulosa cells with the antrum [37,41,43,44].

The morphological integrity of the follicle was graded as follows: 1) primordial/primary follicle: grade 1 (G1), spherical with even distribution of the granulosa cells; grade 2 (G2), granulosa cells are pulled away from the edge of the follicle, but the oocytes are still spherical; and grade 3 (G3), pyknotic nuclei, misshapen oocytes, or vacuolation; and 2) secondary/antral follicle: G1, intact spherical follicle with evenly distributed granulosa and theca cells, small spaces, and spherical oocytes; G2, intact theca cells, disrupted granulosa cells, and spherical oocytes; and G3, disruption and loss of granulosa and theca cells, pyknotic nuclei, and missing oocyte. Under light microscopy (Nikon, Tokyo, Japan) of 400× magnifications, only follicles with visible oocytes were counted and classified to avoid miscounting. Since primordial follicles are an important indicator of ovarian reserve, their integrity was assessed separately. In the present study, we conducted this experiment at least five times to evaluate the statistical significance.

2.7. Evaluation of follicle apoptosis

Apoptosis of ovarian follicles was evaluated by TUNEL assays using an In Situ Cell Death Detection Kit (Roche, Basel, Switzerland) as previously described [39]. Briefly, the tissue sections were deparaffinized, rehydrated and incubated with ready-to-use proteinase K solution (Dako, Hovedstaden, Denmark) for 15 min at room temperature. Following incubation, the slides were treated with TUNEL reaction mixture in a humidified dark chamber for 1 h at 37 °C. After that, the slides were mounted using the VECTASHIELD® Mounting Medium with 4′,6-diamidino-2-phenylindole (Vector Laboratories, Burlingame, CA, USA) and examined under the inverted Zeiss AX10 microscope (Carl Zeiss, Oberkochen, Germany) at 400× magnifications. The cells that had fragmented DNA emitted green fluorescence, while normal cells emitted blue fluorescence. Follicles with over 30% of apoptosis-positive cells or oocyte nuclei (emitting a green signal) were considered as apoptotic, as described previously [40,45].

2.8. Immunostaining of γH2AX and Rad51 at sites of DNA DSBs in mouse OTs

The effects of nfeAFPs on DNA damage and repair were respectively investigated using the biomarkers γH2AX and Rad51. For target antigen retrieval, prepared slides were microwave-heated (700 W) in pH 9.0 Tris/EDTA buffer (DAKO) for 20 min, following peroxidase-blocking solution (DAKO) treatment, which was conducted to inactivate the endogenous horseradish peroxidase for 10 min. For the next step, γH2AX (1:100; Millipore, Millipore, Burlington, MA, USA) and Rad51 (1:100; Bioworld Technology, St. Louis Park, MN, USA) antibodies were added to the different slides, respectively, for 1 h at RT. Secondary Alexa 594 (1:1000; Life Technology, Carlsbad, CA, USA) antibody treatment was performed for 1 h at RT and counterstained with VECTASHIELD® Mounting Medium with 4′,6-diamidino-2-phenylindole (Vector Laboratories). All slides were examined under an inverted Zeiss AX10 microscope (Carl Zeiss) at 400× magnification. Follicles with at least one γH2AX (+) nucleus were considered as follicles with DNA DSBs. In the same way, follicles containing at least one Rad51 (+) nucleus were regarded as follicles with DNA repair [14,40,45,46].

2.9. Statistical analysis

The chi-square test was performed for follicle integrity, apoptosis and DNA DSB/repair ratios using the SPSS version 12.0 software (SPSS Inc., Chicago, IL, USA). The results were considered significantly different when the P value was < 0.05.

2.10. NMR experiments

For NMR experiments, the purified proteins were concentrated to 1 mM in a 90% H_2O/10% D_2O buffer containing 10 mM sodium phosphate (pH 6.0) and 100 mM NaCl. All of the ^{1}H, ^{13}C, and ^{15}N NMR experiments were performed on an Agilent DD2 700-MHz spectrometer (GNU, Jinju, Korea) or a Bruker Avance-III 800-MHz spectrometer (KBSI, Ochang, Korea) equipped with a triple-resonance cryogenic probe. All three-dimensional (3D) triple-resonance experiments were carried out with 1 mM ^{13}C, ^{15}N-labeled wt nfeAFP11 and wt nfeAFP6. All 2D $^{1}H/^{15}N$-HSQC, 3D NOESY-$^{1}H/^{15}N$-HSQC and 3D TOCSY-$^{1}H/^{15}N$-HSQC spectra for wt and mutant nfeAFPs were obtained using 1 mM ^{15}N-labeled protein samples. 2D and 3D data were processed with NMRPIPE [47] and analyzed with SPARKY [48].

The ^{1}H, ^{13}C, and ^{15}N backbone resonance assignments for wt nfeAFP11 and wt nfeAFP6 were obtained from the following 3D experiments: CACB(CO)NH, HNCACB, HNCO, NOESY-$^{1}H/^{15}N$-HSQC, and TOCSY-$^{1}H/^{15}N$-HSQC. The ^{1}H and ^{15}N backbone resonance assignments for nfeAFP11_tri and nfeAFP6_tri were obtained from the 3D NOESY-$^{1}H/^{15}N$-HSQC and TOCSY-$^{1}H/^{15}N$-HSQC experiments. The $^{1}H/^{15}N$ chemical shift changes ($\Delta\delta_{avg}$) were calculated using the following equation:

$$\Delta\delta_{avg} = \sqrt{(\Delta\delta_H)^2 + (\Delta\delta_N/5.88)^2} \quad (1)$$

where $\Delta\delta_H$ and $\Delta\delta_N$ are ^{1}H and ^{15}N chemical shift changes between the wt and utant nfeAFPs, respectively. Backbone dynamics parameters, including longitudinal R_1 relaxation rates, transverse R_2 relaxation rates, and $\{^{1}H\}$-^{15}N heteronuclear NOEs were measured using ^{15}N-labeled wt and mutant nfeAFPs at 5 °C. R_1 values were measured in a series of spectra with relaxation delays of 50, 100, 150, 200, 250, 300, 350, 400, 500, and 600 ms. R_2 measurements were taken with relaxation delays of 10, 30, 50, 70, 90, 110, 130, 150, 190, and 230 ms. For evaluation of $\{^{1}H\}$-^{15}N heteronuclear NOE values, three different data sets with and without an initial proton saturation (2.5-s period) were measured.

3. Results

3.1. TH activity of nfeAFPs

Previous study [27] reported that an QAE1 isoform (wt nfeAFP8) from *Zoarces elongatus Kner* shows full TH activity (Fig. 2). A $QAE2^{ACT}$ mutant of the QAE2 isoform (nfeAFP11_tri), which bears substitution V9Q/V19L/G20V (Fig. 1C), exhibits TH and IRI effects similar to those of its paralogue QAE1 (Fig. 2) [25]. In this study, a triple mutant (SP^{ACT}) of the inactive SP isoform (nfeAFP6_tri) is prepared by of P19, A20, and G42 on the IBS with the corresponding residues (L19, V20, and S42) of the QAE1 isoform (Fig. 1D). Interestingly, this mutant exhibits remarkable TH activity, similar to that of wt nfeAFP8 (Fig. 2). As the temperature decreased below T_m, the crystal growth of the ice bipyramid in nfeAFP6_tri solution

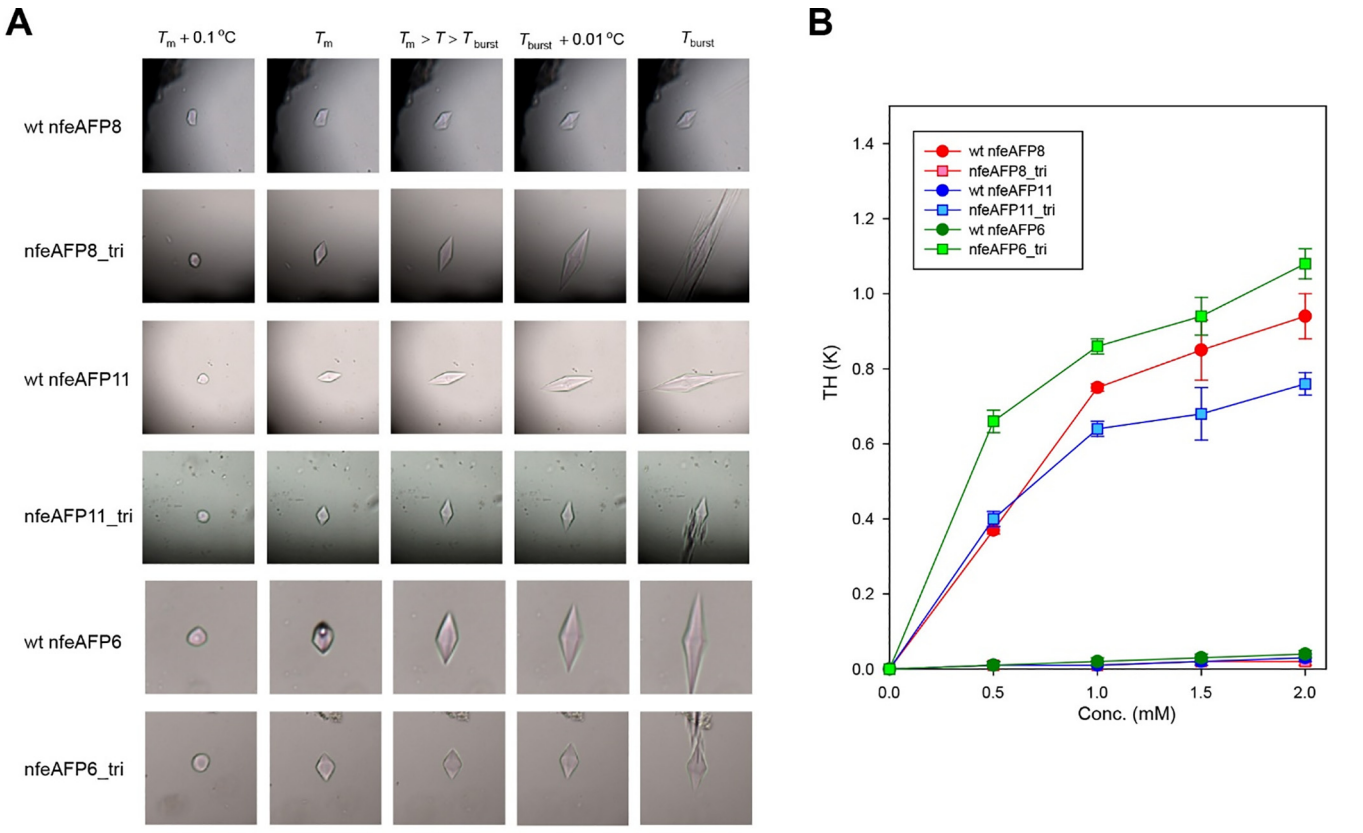

Fig. 2. TH activity of nfeAFPs. (A) Morphological change in an ice crystal observed for 1 mM solutions of wt nfeAFP8 [27] nfeAFP8_tri [27] wt nfeAFP11, nfeAFP11_tri, wt nfeAFP6, and nfeAFP6_tri. Photomicroscope images were obtained at a cooling rate of 0.01 °C·min^{-1}. T_{burst} is defined as the temperature at which crystals rapidly expand. (B) TH activities of wt and mutant AFPs as a function of each total concentration. TH is defined as the absolute value of the difference between T_m and T_{burst}.

was strongly inhibited (the sixth row of the third column in Fig. 2A). However, wt nfeAFP11 and wt nfeAFP6 are incapable of stopping the growth of an ice bipyramid below T_m (Fig. 2A). The bursting elongation of wt nfeAFP11 and wt nfeAFP6 was accompanied by rapid crystal expansion (the third and fifth rows of the third column in Fig. 2A). Thus, these two isoforms had much smaller TH values (= $|T_m - T_{burst}|$) than wt nfeAFP8, nfeAFP11_tri, and nfeAFP6_tri, because $T_m \sim T_{burst}$, where T_{burst} is the bursting temperature. The difference in the IBS is that the inactive isoforms, wt nfeAFP11 and wt nfeAFP6, have V/V/G/S and Q/P/A/G at positions 9/19/20/42, respectively, but the active AFPs, wt nfeAFP8, nfeAFP11_tri, and nfeAFP6_tri have Q/L/VS. These results indicates that the sequence of the IBS is very important for the ACW network formation that is related to the TH activity of type III AFPs.

3.2. IRI activity of nfeAFPs

Fig. 3 shows IRI activities of the three wt isoforms of nfeAFP, nfeAFP8, nfeAFP11, and nfeAFP6, and their triple mutants, nfeAFP8_tri, nfeAFP11_tri, and nfeAFP6_tri. The first row of Fig. 3 indicates the polycrystalline ice created by rapid freezing at −30 °C; this is the expected result of IRI activity. Because the coverslips were flash-frozen at a higher temperature than −70 °C of previous report [35] ice crystals exhibited leaf shapes rather than round or bipyramidal shapes in contrast to the TH results as shown in Fig. 2. At −6 °C, compared with the BSA control, all AFP samples displayed IRI over the first 30 min (second row of Fig. 3). However, after 4 h at −6 °C, the wt nfeAFP11, wt nfeAFP6, and nfeAFT8_tri (inactive mutant of nfeAFP8) demonstrated lower IRI activity with some ice crystal growth, whereas wt nfeAFP8 and the nfeAFP11_tri and nfeAFP6_tri mutants still exhibited significant IRI effects (third row of Fig. 3).

3.3. Morphological evaluation of ovarian follicles

In order to demonstrate that AFPs preserve tissue quality by preventing structural and genetic disruption, we added the different AFPs to the vitrification and warming solutions as indicated in Fig. 4A. Following the vitrification-warming process, the ovarian tissues were histologically analyzed. A total of 22,286 mouse ovarian follicles were evaluated for the proportion of morphologically intact (G1) follicles, both for all collected follicles and for the subset of primordial follicles. In terms of primordial follicles, the vitrified-warmed control showed the lowest proportion of intact follicles (54.1%); however, the proportions were significantly increased to a range of 61 – 70% in the AFP-treated groups, except for the nfeAFP8_tri group (58.7%) (Fig. 4A). Primordial follicles in OTs incubated with AFPs with high TH and IRI activity, i.e., wt nfeAFP8, nfeAFP6_tri, and nfeAFP11_tri, had significantly higher proportions of intact follicles than those incubated with inactive AFPs (wt nfeAFP6, wt nfeAFP11, and nfeAFP8_tri) (Fig. 4A).

Similarly, the proportion of total follicles that were morphologically intact was higher in the AFP-treated samples, with a range of 52 – 63%, whereas the proportion of intact follicles in the vitrified-warmed control was only 37.5% (Fig. 4A). As with the subset of primordial follicles, the proportion of intact total follicles was highest when treated with AFPs with high TH and IRI activity and lowest when treated with the inactive AFPs (Fig. 4A).

3.4. Evaluation of apoptotic follicle ratios

To evaluate the efficiency of cryopreservation of ovarian follicles, we assessed the ability of AFPs to prevent ovarian follicular apoptosis. Exposure to AFPs significantly decreased the proportion of apoptotic follicles (17 – 27%) compared with the vitrified-

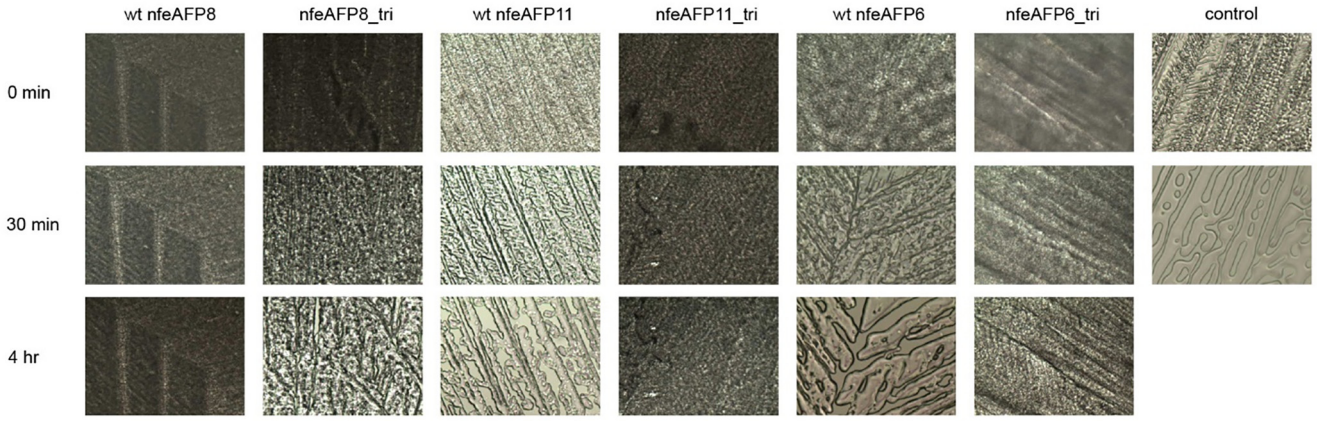

Fig. 3. IRI assessment of nfeAFPs. Ice crystal images collected after complete freezing at −30 °C for 5 min (row 1) and after 30 min (row 2) and 4 h (row 3) at −6 °C. Images show recrystallization of the AFP-containing solutions as indicated. BSA was used as a negative control.

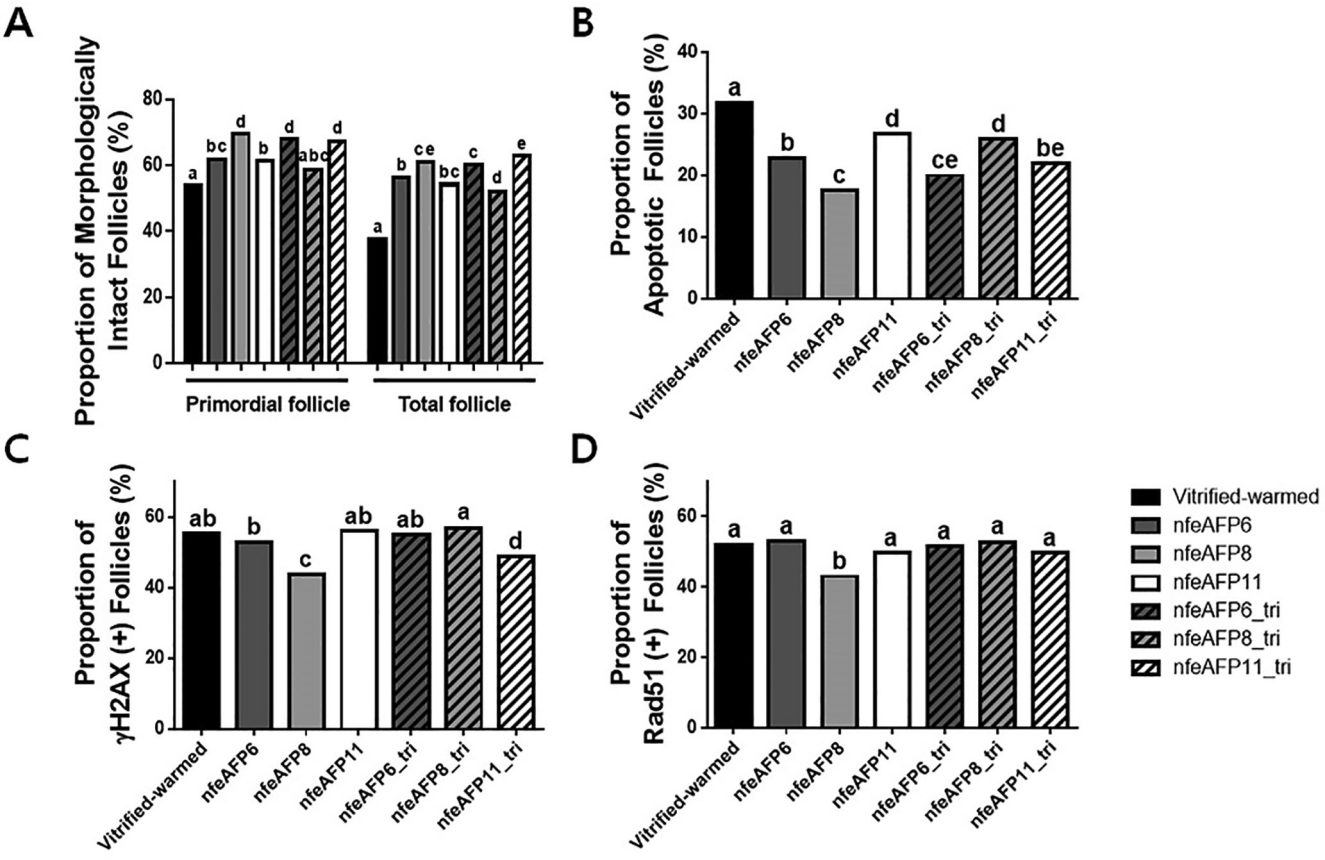

Fig. 4. Beneficial effects of nfeAFPs on mouse ovarian tissue preservation upon vitrification and warming. Preservative effects were quantified in terms of on (A) intact follicle morphology and (B) ovarian follicle apoptosis. Follicle stability was assessed by (C) DNA DSBs, detected via γH2AX staining, and (D) DNA repair activity, measured by staining for Rad51. Different superscript letters indicate significant difference ($P < 0.05$).

warmed control (31.7%) as shown in Fig. 4B. Notably, the nfeAFP8-treated OTs had the lowest proportion of apoptotic follicles (Fig. 4B). In addition, the OTs treated with the QAE2^{ACT} (nfeAFP11_tri) and SP^{ACT} mutants (nfeAFP6_tri) showed significant differences from the other nfeAFP-treated samples, which had no TH and IRI activity (Fig. 4B).

3.5. Evaluations of DNA DSBs and repair

Next, we assessed the number of DNA DSBs, as indicated by detection of γH2AX, and DNA repair activity, as indicated by Rad51 staining, in the follicles of OTs treated with AFPs. The nfeAFP8- and nfeAFP11_tri-treated samples had lower proportions of γH2AX–positive follicles (43.6% and 48.9%, respectively), indicating a relatively lower level of DSBs than the other groups (52 – 57%) (Fig. 4C). The nfeAFP8-treated group had a significantly lower proportion of Rad51-positive follicles (43.0%) than the other groups (49 – 53%) (Fig. 4D). Representative images of hematoxylin and eosin staining, terminal deoxynucleotidyl transferase dUTP nick end labelling (TUNEL) assays, and immunohistochemistry for γH2AX and Rad51 are shown in Supplementary Data Fig. S1.

3.6. Assignment of amide backbone resonances of wt and mutant nfeAFPs

To investigate the structural features of the AFP isoforms that give rise to their differing cryopreservative characteristics, NMR studies of wt nfeAFP8, nfeAFP8_tri, wt nfeAFP11, nfeAFP11_tri, wt nfeAFP6, and nfeAFP6_tri were performed to compare the effects of mutations in the IBS on the 3D structures of AFPs. Amide backbone resonance assignments for wt nfeAFP11 and wt nfeAFP6 were made by heteronuclear NMR experiments [NOESY-^{1}H/^{15}N-HSQC, TOCSY-^{1}H/^{15}N-HSQC, HNCACB, and CACB(CO)NH]. The amide backbone resonances of nfeAFP11_tri and nfeAFP6_tri were assigned by comparing their 3D NOESY-^{1}H/^{15}N-HSQC and TOCSY-^{1}H/^{15}N-HSQC spectra with those of wt nfeAFP11 and wt nfeAFP6, respectively. Amide backbone resonance assignments for wt nfeAFP8 and nfeAFP8_tri were previously reported [27]. Chemical shifts of all the assigned backbone resonances for wt nfeAFP8, nfeAFP8_tri, wt nfeAFP11, nfeAFP11_tri, wt nfeAFP6, and nfeAFP6_tri are listed in Supplementary Data Tables S1 – S3.

The superimposed ^{1}H/^{15}N-HSQC spectra for wt and mutant nfeAFP11 and nfeAFP6 proteins at 5 °C are shown in Supplementary Data Figs. S2 and S3, respectively. In nfeAFP8_tri, the Q9V, L19V, and V20G mutations caused significant chemical shift changes (δ_{avg} > 0.06 ppm) in residues L10, I11, M21, M22, and L51, which are located close to the mutated residues (Fig. 5A, B) [27]. The nfeAFP8_tri mutant also displayed chemical shift changes > 0.06 ppm at residues Q2 and A3 compared to the wt nfeAFP8 (Fig. 5A), probably due to the position of the histidine tag at the N-terminus versus the C-terminus, respectively [27]. Similarly, in nfeAFP11_tri, the V9Q, V19L, and G20V mutations caused chemical shift changes > 0.06 ppm in only residues L10, I11, M51, and G52 (Fig. 5A, C). In contrast, the P19L, A20V, and G42S mutations in nfeAFP6_tri caused systemic perturbation in the HSQC spectrum of nfeAFP6. Residues A16 – T18, M21, M22, S38 – V41, and K43 underwent significant chemical shift changes > 0.06 ppm (Fig. 5A, D). In addition, residues G2 – T8 of the β1 strand, I11 – N14, E23 – K25 of the β2 strand, I32 – A35 of the second 3_{10} helix, and G52 also experienced significant chemical shift changes, even though these residues are far from the mutated residues (Fig. 5D). These results indicated that the triple mutation of nfeAFP6 caused unusual backbone conformational changes in the β1 and β2 strands and the second 3_{10} helix, unlike the mutations in nfeAFP8 and nfeAFP11.

3.7. NOESY-^{1}H/^{15}N-HSQC spectra of wt nfeAFP6 and nfeAFP6_tri

Fig. 6 depicts the expansion of NOESY-^{1}H/^{15}N-HSQC spectra showing the NOE cross-peak of the amide protons of the first 3_{10} helix and β2 strand in wt nfeAFP6 and nfeAFP6_tri. In the inactive wt nfeAFP6, the A20 – M22 amide protons showed NOE cross-peaks with the solvent water resonance but had no NOE interactions with the T18-Hγ1 resonance (Fig. 6A). However, the active nfeAFP6_tri mutant displayed the T18-Hγ1 resonance at 5.04 ppm, which showed significant NOE cross-peaks with the amide protons of T18 – M22 (Fig. 6B). A previous study found that the T18 – M22 amide protons in wt AFP8 showed significant NOE cross-peaks with the T18-Hγ1 resonance at 5.09 ppm [27]. A similar result was observed for the active mutant of nfeAFP11, nfeAFP11_tri [26]. However, like nfeAFP6, the inactive nfeAFP11 isoform [26] and the nfeAFP8_tri mutant [27] do not have these NOE interactions. Instead, in these AFPs, the T18 amide protons showed NOE cross-peaks with a solvent water resonance [26,27]. These results indicate that the T18 side-chain of the active QAE1 isoform exhibits unique H-bonding interactions, which are disrupted in the inactive QAE2 and SP isoforms.

In wt nfeAFP6, the F34 side-chain showed strong NOE cross-peaks with the amide protons of residues G24 and K25 of the β2 strand (Fig. 6C). In addition, this side-chain also exhibited weak

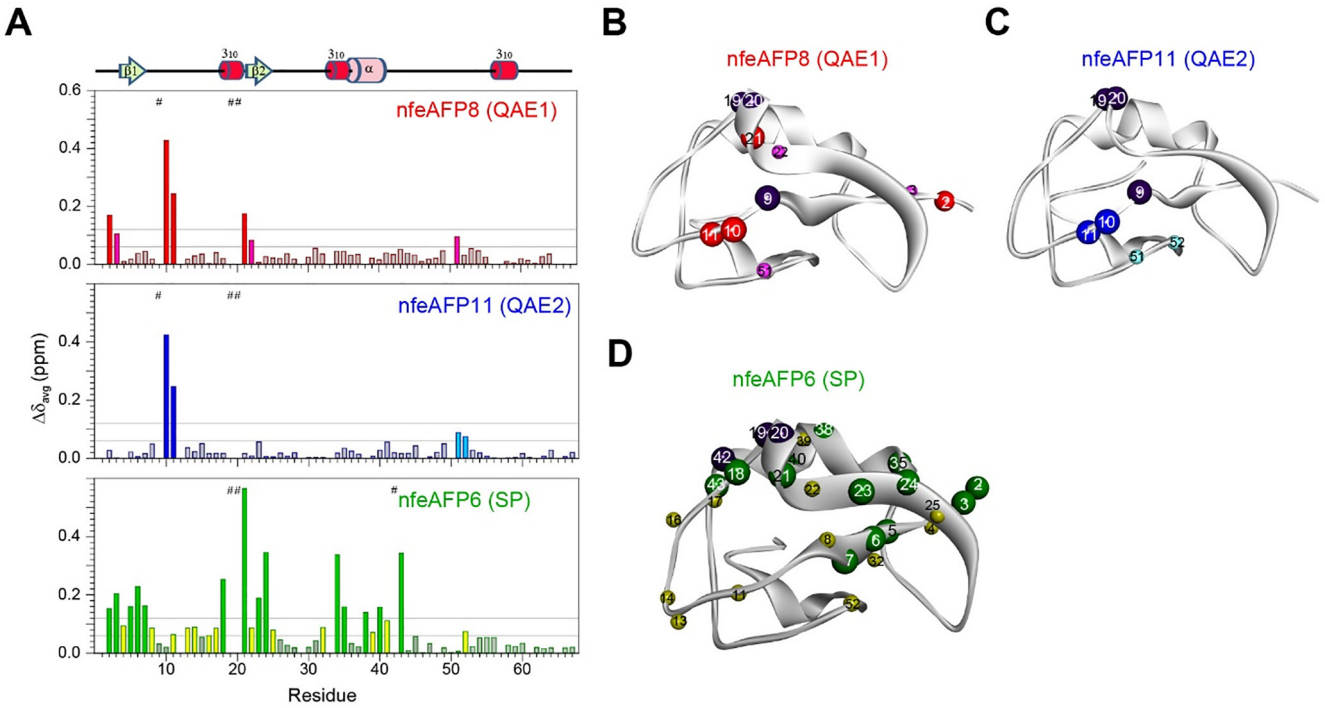

Fig. 5. Chemical shift differences between wt and mutant nfeAFPs. (A) The weighted average ^{1}H/^{15}N chemical shift changes ($\Delta\delta_{avg}$) between the wt and mutant nfeAFP8, nfeAFP11, and nfeAFP6. # symbols indicate the disappearance of the peak upon mutation. 3D structures of (B) nfeAFP8 (PDB id = 1HG7), (C) nfeAFP11 (PDB id = 2LX2), and (D) nfeAFP6 (PDB id = 1OPS) are shown. Dark purple color indicates the mutated residues in each nfeAFP isoform. Colors used to illustrate ^{1}H/^{15}N chemical shift changes ($\Delta\delta_{avg}$) between the wt and mutant nfeAFPs: red, blue, and green, >0.12 ppm; magenta, cyan, and yellow, 0.08–0.12 ppm). (For interpretation of the references to color in this figure legend, the reader is referred to the web version of this article.)

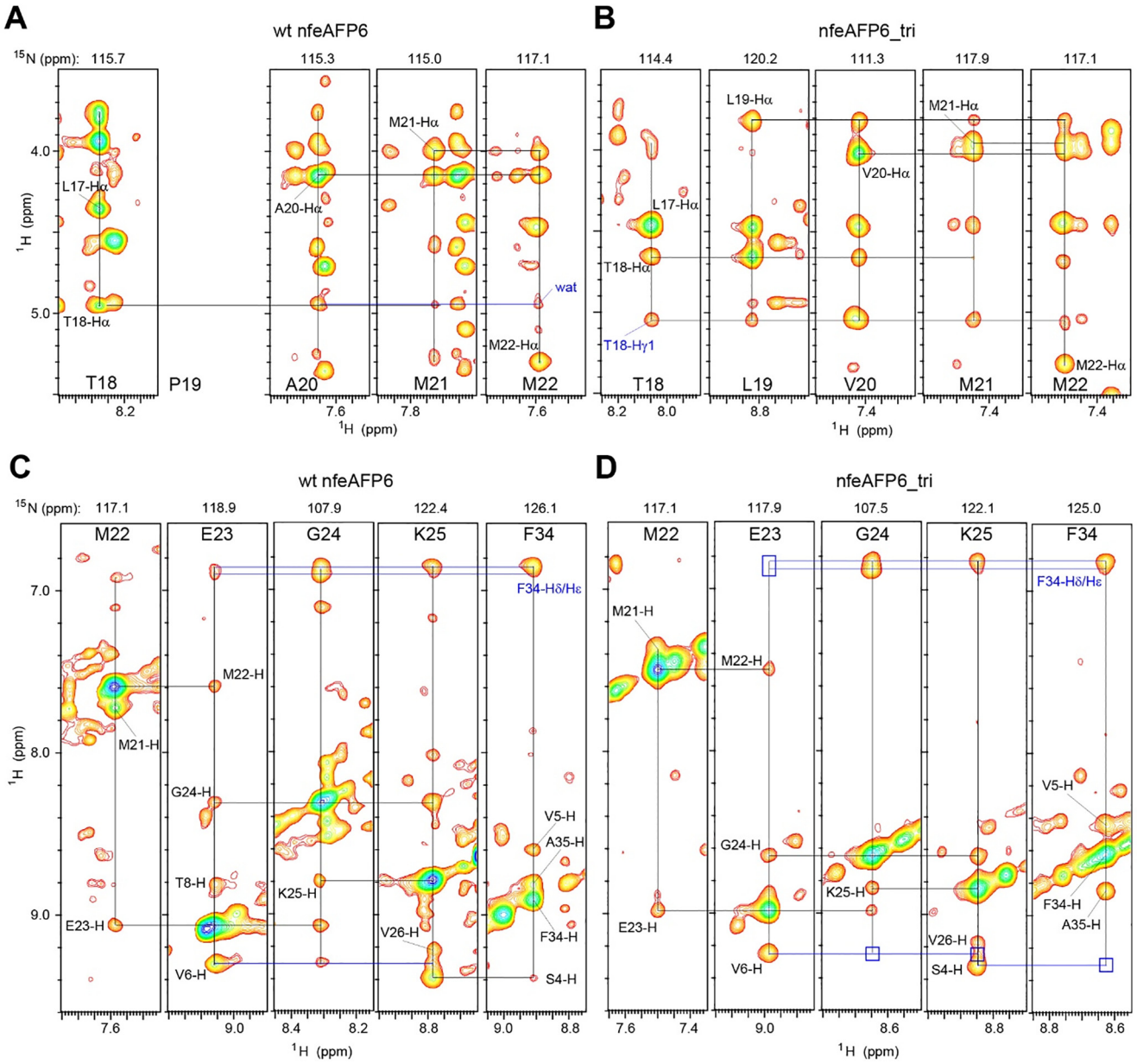

Fig. 6. NOESY-^{1}H/^{15}N-HSQC spectra of the nfeAFP6s. Strip plots of the NOESY-^{1}H/^{15}N-HSQC spectra (mixing time: 160 ms) in (A, C) wt nfeAFP6 and (B, D) nfeAFP6_tri at 5 °C. The data show the cross-peaks aligned to the (A, B) T18, L19, A20/V20, M21, and M22 and (C, D) M22, E23, G24, K25, and F34 amide resonances. Wat indicates the resonance originating from the free water molecules. Rectangles in D show where cross-peaks are lost after the mutations are introduced.

NOEs with the E23 amide proton (Fig. 6C). However, in nfeAFP6_tri, the E23 amide proton had no NOE cross-peak with the F34 side-chain (Fig. 6D). These results indicate that the F34 side-chain has different orientation in the nfeAFP6_tri compared to wt nfeAFP6. In addition, in wt nfeAFP6, the F34 and G24 amide protons showed the NH ↔ NH NOE with the S4 and V6 amide protons, respectively (Fig. 6C), whereas nfeAFP6_tri did not show these NOEs (Fig. 6D). These NOE data indicate that the wt nfeAFP6 displays a distinct conformation of the first 3_{10} helix and β2 strand compared to the active QAE1 isoform of nfeAFP6; these features are correlated with the unusual chemical shift changes of nfeAFP6 upon the P19L/A20V/G42S mutations described above. Taken together, this distinct conformation explains why the SP isoform exhibits a lower TH and IRI activity than the QAE1 isoform.

3.8. Backbone dynamics of wt and mutant nfeAFPs

Next, in order to understand why the QAE2 isoform displays low TH and IRI activity, even though its IBS is similar in conformation to the QAE1 isoform, we determined the longitudinal R_1 relaxation rates, transverse R_2 relaxation rates, and {^{1}H}-^{15}N heteronuclear NOEs for wt and mutant nfeAFPs (Supplementary Data Fig. S4). Interestingly, in the inactive isoform, wt nfeAFP11, the R_2/R_1 ratio of G20 is significantly larger than the average value (Fig. 7A). We further analyzed the products R_1R_2 to clarify the structural flexibility, because the R_2/R_1 ratio has both the structural flexibility and anisotropic motion information [49]. The wt nfeAFP11 has much larger R_1R_2 value for G20 with an NOE value of 0.86 ± 0.03 than the average value at a magnetic field strength

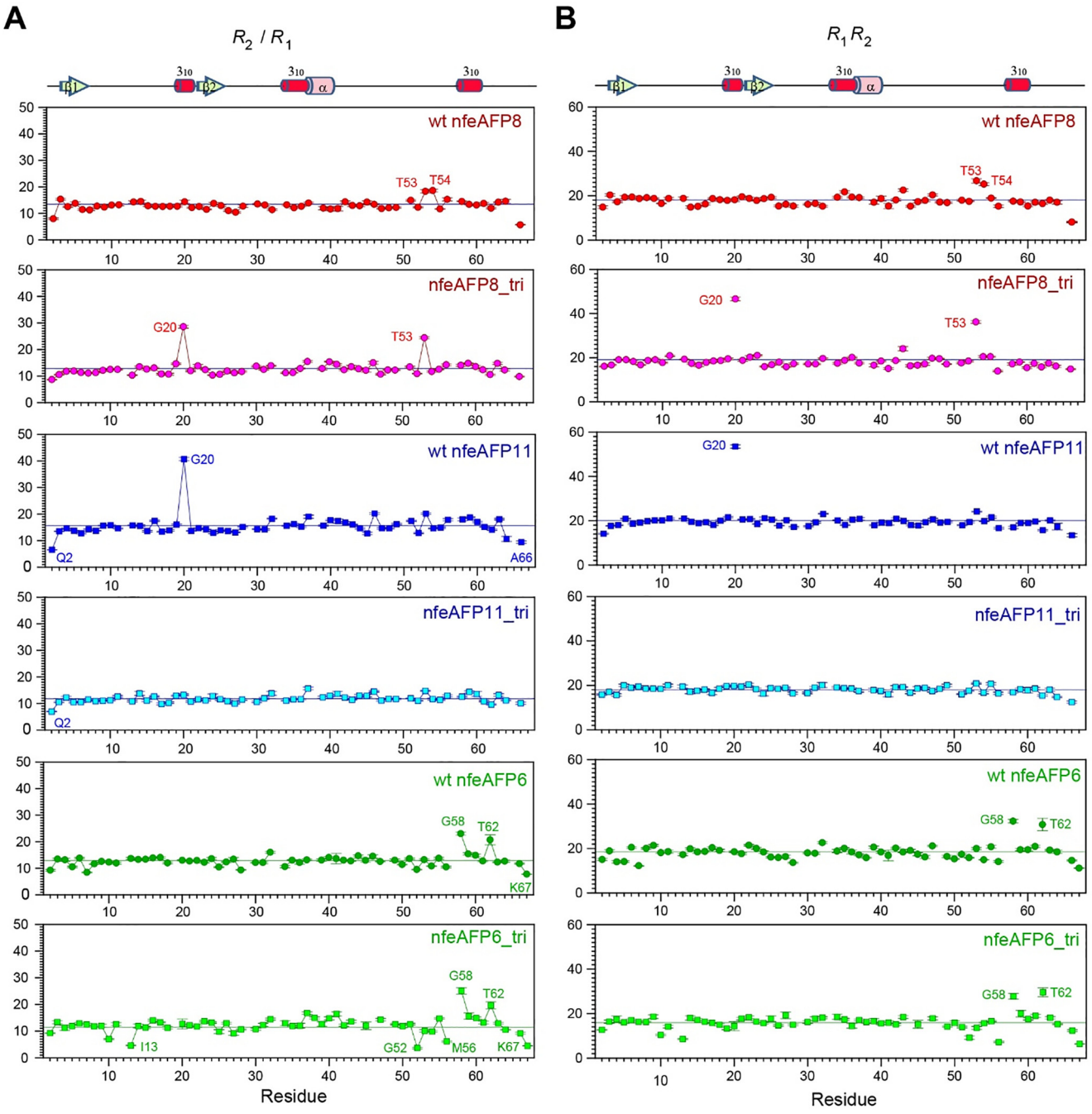

Fig. 7. Backbone dynamics of nfeAFPs. (A) R_2/R_1 and (B) R_1R_2 values of wt nfeAFP8, AFP8_tri, wt nfeAFP11, nfeAFP11_tri, wt nfeAFP6, and nfeAFP6_tri at 5 °C. The error bars represent curve fitting errors during the determination of R_1 and R_2 values from experimental data.

of 16.4 T (Fig. 7B), indicating conformational flexibility of the first 3_{10} helix on the μs – ms timescale. Similarly, the inactive mutant of nfeAFP8, nfeAFP8_tri, which was previously studied [27] also had a significantly large R_1R_2 value of G20 with an NOE value of 0.85 ± 0.04 at a field strength of 16.4 T (Fig. 7B). These results indicate that both the wt nfeAFP11 and nfeAFP8_tri exhibit conformational flexibility in the first 3_{10} helix, which might explain their lower TH and IRI activity.

The inactive nfeAFP6 isoform does not display this kind of flexibility (Fig. 7A), perhaps because the P19 residue introduces backbone rigidity into the first 3_{10} helix. In addition, the active mutants, nfeAFP11_tri and nfeAFP6_tri, also show no clear backbone conformational flexibility of the first 3_{10} helix (Fig. 7).

4. Discussion

The type III AFPs are classified as QAE1, QAE2, and SP isoforms [23,24]. The QAE1 isoform is able to bind to both the primary prism and pyramidal planes of ice [50]. This isoform is capable of stopping the growth of ice crystals and exhibits full TH and IRI activity (Figs. 2 and 3). However, the QAE2 and SP isoforms can bind to only the pyramidal plane [50] and are incapable not only of stopping ice growth but also of inhibiting ice recrystallization (Figs. 2 and 3). Thus, the ability to bind to the primary prism plane of ice crystals is thought to be the very important for the TH and IRI activity.

The QAE2 isoform nfeAFP11 differs from the QAE1 isoform nfeAFP8 by four residues positioned at the prism plane binding

surface (residues 9, 19, 20, and 41) (Fig. 1). A previous study revealed that replacement of residues 9, 19, and 20 in nfeAFP8 with the corresponding residues of nfeAFP11 converted the active isoform into an inactive AFP (called a QAE1^{INACT}) [27]. This QAE1^{INACT} (nfeAFP8_tri) lost both TH and IRI activity (Figs. 2 and 3). Conversely, the inactive QAE2 isoform can be converted to a fully active AFP (called a QAE2^{ACT}) by mutation of the same three residues [25]. In the case of the SP isoform nfeAFP6, the prism plane binding surface has three residues (19, 20, and 42) that differ from the corresponding plane of nfeAFP8 (Fig. 1). The current study found that replacement of these residues in nfeAFP6 with the corresponding residues of nfeAFP8 converted it to a fully active SP^{ACT} (Figs. 2 and 3).

In order to connect the TH and IRI activities of AFPs and their biological effects, we also studied the effects of the wt and mutant nfeAFPs on mouse OT cryopreservation. As expected, the three active AFPs (nfeAFP8, nfeAFP11_tri, and nfeAFP6_tri) preserved significantly higher proportions of intact ovarian follicles than the QAE2 and SP isoforms or the control solution (Fig. 4A). A similar pattern was also observed in the apoptosis data of ovarian follicles incubated with AFPs (Fig. 4B). This means that the specific mutations made to the inactive nfeAFP11 and nfeAFP6, which converted them into active AFPs, could not completely recover the protective capacity of wt nfeAFP8. For better understanding of the effect of AFPs on follicular apoptosis, more systematic biophysical and cryopreservation studies are required.

The mechanism that AFPs protect ovarian tissue during vitrification is not fully known. In the present study, mutants that has higher TH and IRI activity showed better cryoprotective results. TH activity is not the main mechanism of cryoprotection because ice formation can occur when temperature is decreased to below TH gap. During vitrification, theoretically ice formation does not occur thus ice recrystallization during warming is the main cause of cryodamage. Previous study showed that IRI during the warming procedure is critical to the cryoprotective outcomes of the vitrification-warming of ovarian tissue [15]. Other previous studies demonstrate that TH activity was not necessarily translated into improvements in the cryopreservation efficiency of biological samples [51,52]. Interaction with membrane is another possible cryoprotective mechanism of AFPs. One mechanism of cell damage at low temperature is thermotropic phase transition partly due to weakened hydrophobic interactions. When the transition from liquid crystalline to gel phase occurred, cell membranes become leaky, resulting in cell death [53]. Rubinsky et al. proved AFPs protect cell membrane during hypothermic storage [54].

Cryodamage involves mechanical and osmotic stress and induces DNA DSBs followed by severe or lethal mutations of cells [55,56]. In this study using mouse OT, the proportions of γH2AX (+) follicles were significantly decreased in the active AFP-treated samples compared with the sham control-treated and the inactive AFP-treated samples. This study demonstrated that nfeAFP8 (high TH and IRI) was superior in protecting follicles form DNA damage, leading to decreased need for DNA repair during cryopreservation of OT. In the case of the nfeAFP6_tri and nfeAFP11_tri mutants, they had high TH and IRI activities but did not improve DNA damage/repair as much as nfeAFP8, and this could be due to the limitations of mutant AFPs. Only wt nfeAFP8 with high TH and high IRI activities showed remarkably improved outcomes in all evaluations in this study when compared to the vitrified-warmed control. These results suggest that supplementation of the vitrification and warming media for cryopreservation of OT with the native QAE1 isoform, especially nfeAFP8, would be a promising approach for patients who need to preserve their fertility.

In the present study, ovarian tissues were exposed to high concentration of cryoprotective agents (CPAs) which induce an inevitable osmotic shock in cells and tissue. Increased ROS generation is associated with osmotic stress in a variety of somatic cells as well as in sperm and may serve as a signaling mechanism responsible for the cell adaptive response [57,58]. Notably, cryopreservation process also creates abundant amount of ROS in oocytes, spermatozoa, somatic cells and tissues [12,58,59]. In our previous study, vitrification media supplemented with different types of AFPs decrease the ROS production in mouse oocyte and it may result in a reduction of DSBs [12]. Collectively, AFPs in cryopreservation and warming media might modulate osmotic injuries during ovarian tissue cryopreservation and eventually show the protective effects in terms of intracellular DNA damage. However, further studies how AFPs decrease ROS production would be required.

As described above, for the efficient cryopreservation of mouse OT achieved by supplementation of AFPs, the AFPs must stop the growth of ice crystals and efficiently inhibit ice recrystallization. The QAE1 isoform, which has high TH and IRI activities, can bind to both the primary prism and pyramidal planes of hexagonal ice crystals, whereas the QAE2 and SP isoforms bind solely to the pyramidal plane (*see* Fig. 8) [25,50]. Comparison of the conformation and dynamics of the QAE1 isoform with the inactive QAE2 and SP isoforms can explain the strong binding affinity of the QAE1 AFPs to the prism plane of ice crystals (summarized in Fig. 8). First, in the QAE1 isoform, the L19 and V20 amide protons and the T18 γ-OH of the QAE1 isoform play an important role in anchoring water molecules (#78, #80, and #81 in Fig. 8), which might be considered the ACW cluster that space-match to the primary prism plane of the ice crystal. The same H-bonding interaction was also observed in the QAE2^{ACT} tetra-mutant (V9Q/V19L/G20V/I41V) [25]. This structural feature is consistent with the observation of the T18-Hγ1 resonance and absence of NOEs of the L19 and V20 amide protons with the solvent water resonance in wt nfeAFP8 [27]. In addition, the QAE2^{ACT} (nfeAFP11_tri) [26] and SP^{ACT} mutants (nfeAFP6_tri) (Fig. 6B) displayed the same NOE pattern as the wt nfeAFP8. In contrast to wt nfeAFP8, in several QAE1^{INACT} mutants of nfeAFP8 (V20G, L19V/V20G, and nfeAFP8_tri), the T18-Hγ1 resonance is absent and the NH of residues 19 and 20 showed significant NOEs with the solvent water [27]. Similar results were observed for the inactive QAE2 [26] and SP isoforms (Fig. 6A). This NOE pattern is consistent with the structural feature of the QAE2 isoform, in which the amide protons of residues V19 and G20 exhibited H-bond interaction with surface water molecule rather than the ACW network [25]. Recently, it has been reported that the efficiency of TH and IRI activities was determined by the binding affinity of AFPs to a wider area of ice crystal [60]. Taken together, it has been suggested that the disruption of ACW networks in the inactive QAE2 and SP isoforms as well as QAE1^{INACT} mutant reduces the AFP-binding area of ice crystal, resulting in loss of TH and IRI activity.

Second, in the inactive AFPs, QAE2 and QAE1^{INACT}, the first 3_{10} helix, which constitutes the prism plane binding surface, showed a flexible backbone conformation compared to that of the QAE1 isoform (Fig. 8). The inactive AFPs, QAE1^{INACT} (nfeAFP8_tri) and QAE2 (wt nfeAFP11) had a significantly larger R_1R_2 value for G20 than the average value (Fig. 7B), indicating conformational flexibility. The structural study revealed that, in the QAE2 isoform, the amide protons of residues V19 and G20 exhibited H-bond interaction with surface water molecule rather than the ACW network [25]. The larger R_1R_2 value of G20 can be explained by the chemical exchange between the surface water-bound and -unbound conformations. However, the active AFPs, such as QAE1 and QAE2^{ACT}, exhibited the unique H-bonding interaction with two ACW networks which space-match to the primary prism and pyramidal ice planes [25]. Thus, the QAE1 isoform as well as the active mutants, QAE2^{ACT} (nfeAFP11_tri) and SP^{ACT} (nfeAFP6_tri), show no clear backbone conformational flexibility of the first 3_{10} helix

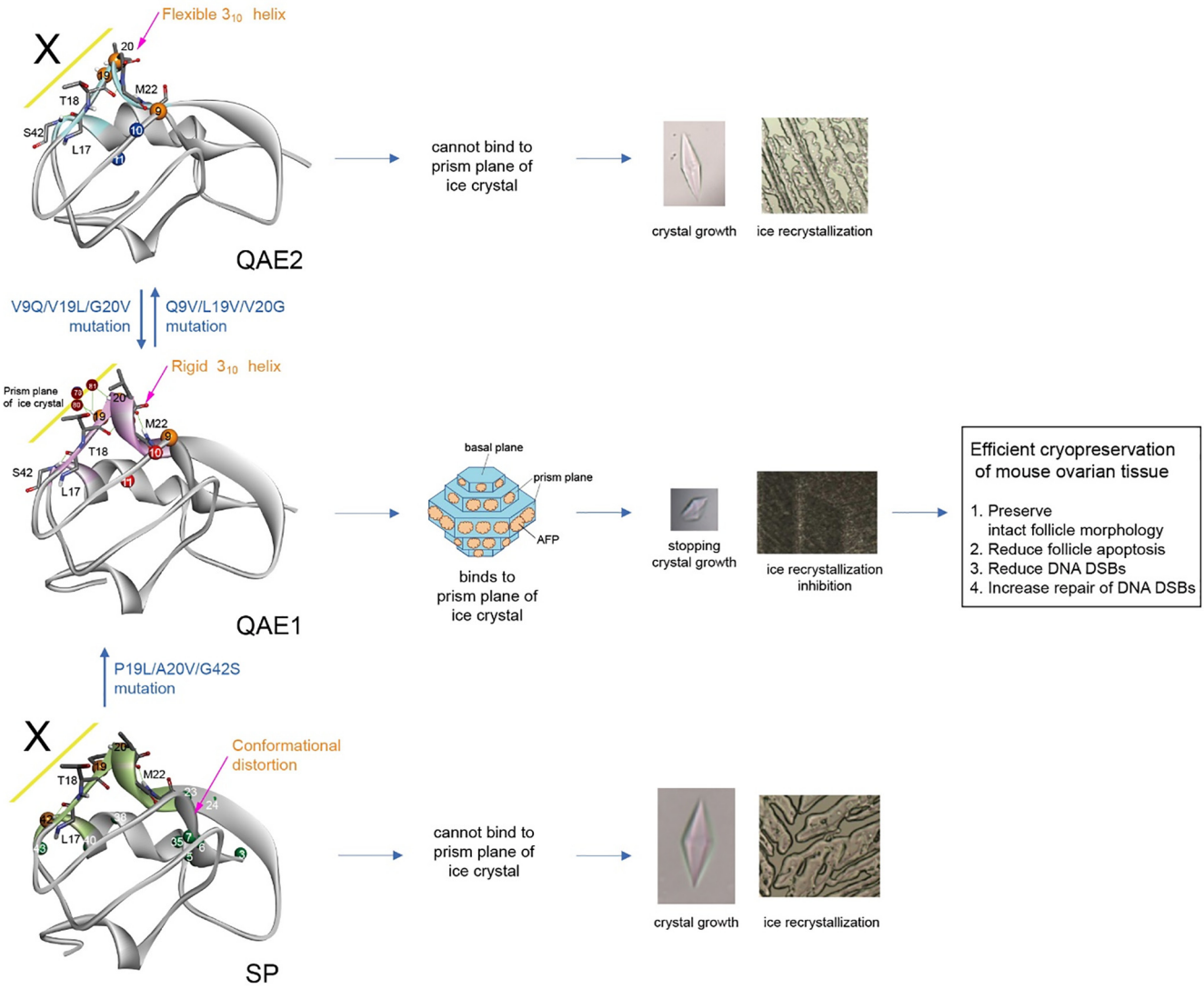

Fig. 8. Summary of cryopreservation activity of type III AFP. The orange color indicates the mutated residues in each AFP isoform. The red, blue, and green colors indicate the residues which show the $\Delta\delta_{avg}$ values of > 0.12 ppm between the wt and mutant AFPs. Water molecules from the 1HG7 PDB entry that match the spacing of waters on the primary prism plane of ice are colored brown and numbered according to the PDB entry. The primary prism plane of ice crystal is colored yellow. The first 3_{10} helix region (residues T18 – M22) and residue 42 are represented by stick view. Green solid lines indicate H-bonding interactions. (For interpretation of the references to color in this figure legend, the reader is referred to the web version of this article.)

(Fig. 7B). The inactive SP isoform (wt nfeAFP6) does not display this kind of flexibility (Fig. 7B) because the P19 residue introduces backbone rigidity into the first 3_{10} helix. It was concluded that, in the inactive AFPs, QAE1^{INACT} and QAE2, the flexible structure of the first 3_{10} helix interferes with the H-bonding interaction between the IBS and the prism plane of ice crystals, thereby preventing full TH and IRI activity.

Third, the inactive SP isoform displays unusual backbone conformational differences in the β1 and β2 strands and the second 3_{10} helix, which constitutes the prism plane binding surface, compared to the active QAE1 isoform (Fig. 8). In nfeAFP6_tri, residues of the β1 and β2 strands and the second 3_{10} helix presented significant chemical shift changes compared to wt nfeAFP6, even though these residues are far from the mutated residues (Fig. 5D). However, in the case of nfeAFP8_tri and nfeAFP11_tri, the triple mutations caused significant chemical shift changes in the residues located close to the mutated residues (Fig. 5). Taken together, it was concluded that the inactive SP isoform exhibits a distinct overall backbone conformation from the active QAE1 isoform, which disrupts the H-bonding interaction of the IBS with the prism plane of ice crystals for full TH and IRI activity.

5. Conclusions

In this study, we have studied the TH, IRI, and cryopreservation activities as well as the structural and dynamic features of the three isoforms of type III nfeAFPs and their IBS mutants. We found that, like the active QAE1 isoform, the QAE2^{ACT} and SP^{ACT} mutants of the inactive isoforms displayed the full TH and IRI effects. Cryopreservation studies of mouse OT revealed that the supplementation of preservation and warming media with the QAE1 isoform and QAE2^{ACT} and SP^{ACT} mutants showed more effective preservation of intact follicles and prevented DNA DSB damage more effectively than other inactive isoforms. NMR studies showed that the QAE1 isoform, including the QAE2^{ACT} and SP^{ACT} mutants, formed unique H-bonds within the first 3_{10} helix that played an important role in the formation of ACW networks for efficient binding to the primary

prism and primary planes of ice crystals, which was disrupted in the inactive isoforms. Our results suggest that the unique conformation of the IBS in the type III AFPs is modulated by specific mutations in the IBS and thus determines the degree of TH, IRI, and cryopreservation activity.

CRediT authorship contribution statement

Seo-Ree Choi: Conceptualization, Data curation, Formal analysis, Writing - original draft. **Jaewang Lee:** Data curation, Formal analysis, Writing - original draft. **Yeo-Jin Seo:** Conceptualization, Data curation, Formal analysis, Writing - original draft. **Hyun Sun Kong:** Data curation, Formal analysis. **Minjae Kim:** Data curation, Formal analysis. **EonSeon Jin:** Data curation, Formal analysis. **Jung Ryeol Lee:** Conceptualization, Formal analysis, Funding acquisition, Writing - original draft, Writing - review & editing. **Joon-Hwa Lee:** Conceptualization, Formal analysis, Funding acquisition, Writing - original draft, Writing - review & editing.

Declaration of Competing Interest

The authors declare that they have no known competing financial interests or personal relationships that could have appeared to influence the work reported in this paper.

Acknowledgements

This work was supported by the National Research Foundation of Korea (2020R1A2C1006909 to J.-H.L.), which is funded by the Ministry of Science and ICT and the Korean Health Technology R&D Project through the Korean Health Industry Development Institute, funded by the Ministry of Health and Welfare (HI18C0081 and HI18C1999 to J.R.L.). This work was also supported by the Samsung Science and Technology Foundation (SSTF-BA1701-10 to J.-H.L.) and a KBSI grant (D39700). We thank Melissa Stauffer, of Scientific Editing Solutions, for editing the manuscript.

Appendix A. Supplementary data

Supplementary data to this article can be found online at https://doi.org/10.1016/j.csbj.2021.01.016.

References

[1] DeVries AL, Wohlschlag DE. Freezing resistance in some Antarctic fishes. Science 1969;163:1073–5.
[2] Yeh Y, Feeney RE. Antifreeze proteins: structures and mechanisms of function. Chem Rev 1996;96:601–18.
[3] Ewart KV, Lin Q, Hew CL. Structure, function and evolution of antifreeze proteins. Cell Mol Life Sci 1999;55:271–83.
[4] Fletcher GL, Hew CL, Davies PL. Antifreeze proteins of teleost fishes. Annu Rev Physiol 2001;63:359–90.
[5] Bowles DJ, Lillford PJ, Rees DA, Shanks IA, Davies PL, Baardsnes J, Kuiper MJ, Walker VK. Structure and function of antifreeze proteins. Phil Trans R Soc Lond B 2002;357:927–35.
[6] Jia Z, Davies PL. Antifreeze proteins: an unusual receptor–ligand interaction. Trends Biochem Sci 2002;27:101–6.
[7] Cheung RCF, Ng TB, Wong JH. Antifreeze proteins from diverse organisms and their applications: an overview. Curr Protein Pept Sci 2017;18:262–83.
[8] Bar Dolev M, Braslavsky I, Davies PL. Ice-binding proteins and their function. Annu Rev Biochem 2016;85:515–42.
[9] Garnham CP, Gilbert JA, Hartman CP, Campbell RL, Laybourn-Parry J, Davies PL. A Ca^{2+}-dependent bacterial antifreeze protein domain has a novel beta-helical ice-binding fold. Biochem J 2008;411:171–80.
[10] Raymond JA, Christner BC, Schuster SC. A bacterial ice-binding protein from the Vostok ice core. Extremophiles 2008;12:713–7.
[11] Lee SG, Koh HY, Lee JH, Kang S-H, Kim HJ. Cryopreservative effects of the recombinant ice-binding protein from the arctic yeast leucosporidium sp. on red blood cells. Appl Biochem Biotechnol 2012;167:824–34.
[12] Lee HH, Lee HJ, Kim HJ, Lee JH, Ko Y, Kim SM, et al. Effects of antifreeze proteins on the vitrification of mouse oocytes: comparison of three different antifreeze proteins. Hum Reprod 2015;30:2110–9.
[13] Lee JR, Youm HW, Lee HJ, Jee BC, Suh CS, Kim SH. Effect of antifreeze protein on mouse ovarian tissue cryopreservation and transplantation. Yonsei Med J 2015;56:778–84.
[14] Lee J, Kim SK, Youm HW, Kim HJ, Lee JR, Suh CS, et al. Effects of three different types of antifreeze proteins on mouse ovarian tissue cryopreservation and transplantation. PLoS One 2015;10:e0126252.
[15] Kong HS, Kim EJ, Youm HW, Kim SK, Lee JR, Suh CS, Kim SH. Improvement in ovarian tissue quality with supplementation of antifreeze protein during warming of vitrified mouse ovarian tissue. Yonsei Med J 2018;59:331–6.
[16] Gandolfi F, Paffoni A, Papassobrambilla E, Bonetti S, Brevini T, Ragni G. Efficiency of equilibrium cooling and vitrification procedures for the cryopreservation of ovarian tissue: comparative analysis between human and animal models. Fertil Steril 2006;85:1150–6.
[17] Jensen AK, Macklon KT, Fedder J, Ernst E, Humaidan P, Andersen CY. 86 successful births and 9 ongoing pregnancies worldwide in women transplanted with frozen-thawed ovarian tissue: focus on birth and perinatal outcome in 40 of these children. J Assist Reprod Genet 2017;34:325–36.
[18] Lee S, Ryu KJ, Kim B, Kang D, Kim YY, Kim T. Comparison between slow freezing and vitrification for human ovarian tissue cryopreservation and xenotransplantation. Int J Mol Sci 2019;20:3346.
[19] Amorim CA, Curaba M, Van Langendonckt A, Dolmans MM, Donnez J. Vitrification as an alternative means of cryopreserving ovarian tissue. Reprod Biomed Online 2011;23:160–86.
[20] Fujihara M, Kaneko T, Inoue-Murayama M. Vitrification of canine ovarian tissues with polyvinylpyrrolidone preserves the survival and developmental capacity of primordial follicles. Sci Rep 2019;9:3970.
[21] Suzuki N, Yoshioka N, Takae S, Sugishita Y, Tamura M, Hashimoto S, et al. Successful fertility preservation following ovarian tissue vitrification in patients with primary ovarian insufficiency. Hum Reprod 2015;30:608–15.
[22] Antson AA, Smith DJ, Roper DI, Lewis S, Caves LSD, Verma CS, et al. Understanding the mechanism of ice binding by type III antifreeze proteins. J Mol Biol 2001;305:875–89.
[23] Hew CL, Wang NC, Joshi S, Fletcher GL, Scott GK, Hayes PH, et al. Multiple genes provide the basis for antifreeze protein diversity and dosage in the ocean pout, Macrozoarces americanus.. J Biol Chem 1988;263:12049–55.
[24] Nishimiya Y, Sato R, Takamichi M, Miura A, Tsuda S. Co-operative effect of the isoforms of type III antifreeze protein expressed in Notched-fin eelpout, Zoarces elongatus Kner. FEBS J 2005;272:482–92.
[25] Garnham CP, Nishimiya Y, Tsuda S, Davies PL. Engineering a naturally inactive isoform of type III antifreeze protein into one that can stop the growth of ice. FEBS Lett 2012;586:3876–81.
[26] Kumeta H, Ogura K, Nishimiya Y, Miura Ai, Inagaki F, Tsuda S. NMR structure note: a defective isoform and its activity-improved variant of a type III antifreeze protein from Zoarces elongates Kner. J Biomol NMR 2013;55:225–30.
[27] Choi S-R, Seo Y-J, Kim M, Eo Y, Ahn H-C, Lee A-R, et al. NMR study of the antifreeze activities of active and inactive isoforms of a type III antifreeze protein. FEBS Lett 2016;590:4202–12.
[28] Garnham CP, Campbell RL, Davies PL. Anchored clathrate waters bind antifreeze proteins to ice. Proc Natl Acad Sci U S A 2011;108:7363–7.
[29] Mahatabuddin S, Fukami D, Arai T, Nishimiya Y, Shimizu R, Shibazaki C, et al. Polypentagonal ice-like water networks emerge solely in an activity-improved variant of ice-binding protein. Proc Natl Acad Sci U S A 2018;115:5456–61.
[30] Choi S-R, Kim N-H, Jin H-S, Seo Y-J, Lee J, Lee J-H. Base-pair opening dynamics of nucleic acids in relation to their biological function. Comput Struct Biotechnol J 2019;17:797–804.
[31] Redfield C. Using nuclear magnetic resonance spectroscopy to study molten globule states of proteins. Methods 2004;34:121–32.
[32] Kobashigawa Y, Nishimiya Y, Miura K, Ohgiya S, Miura A, Tsuda S. A part of ice nucleation protein exhibits the ice-binding ability. FEBS Lett 2005;579:1493–7.
[33] Bravo LA, Griffith M. Characterization of antifreeze activity in Antarctic plants. J Exp Bot 2005;56:1189–96.
[34] Gwak IG, sic Jung W, Kim HJ, Kang S-H, Jin E. Antifreeze protein in Antarctic marine diatom, Chaetoceros neogracile. Mar Biotechnol 2010;12:630–9.
[35] Knight CA, Hallett J, DeVries AL. Solute effects on ice recrystallization: an assessment technique. Cryobiology 1988;25:55–60.
[36] Knight CA, Wen D, Laursen RA. Nonequilibrium antifreeze peptides and the recrystallization of ice. Cryobiology 1995;32:23–34.
[37] Youm HW, Lee JR, Lee J, Jee BC, Suh CS, Kim SH. Optimal vitrification protocol for mouse ovarian tissue cryopreservation: effect of cryoprotective agents and in vitro culture on vitrified-warmed ovarian tissue survival. Hum Reprod 2014;29:720–30.
[38] Kim EJ, Lee HJ, Lee J, Youm HW, Lee JR, Suh CS, et al. The beneficial effects of polyethylene glycol-superoxide dismutase on ovarian tissue culture and transplantation. J Assist Reprod Genet 2015;32:1561–9.
[39] Kong HS, Kim SK, Lee J, Youm HW, Lee JR, Suh CS, et al. Effect of exogenous anti-mullerian hormone treatment on cryopreserved and transplanted mouse ovaries. Reprod Sci 2016;23:51–60.
[40] Lee J, Kong HS, Kim EJ, Youm HW, Lee JR, Suh CS, Kim SH. Ovarian injury during cryopreservation and transplantation in mice: a comparative study between cryoinjury and ischemic injury. Hum Reprod 2016;31:1827–37.
[41] Lee J, Kim EJ, Kong HS, Youm HW, Lee JR, Suh CS, et al. A combination of simvastatin and methylprednisolone improves the quality of vitrified-warmed ovarian tissue after auto-transplantation. Hum Reprod 2015;30:2627–38.

[42] Lundy T, Smith P, O'Connell A, Hudson NL, McNatty KP. Populations of granulosa cells in small follicles of the sheep ovary. Reproduction 1999;115:251–62.
[43] Lee J, Lee JR, Youm HW, Suh CS, Kim SH. Effect of preoperative simvastatin treatment on transplantation of cryopreserved-warmed mouse ovarian tissue quality. Theriogenology 2015;83:285–93.
[44] Youm HW, Lee J, Kim EJ, Kong HS, Lee JR, Suh CS, et al. Effects of Angiopoietin-2 on Transplanted Mouse Ovarian Tissue. PLoS One 2016;11:e0166782.
[45] Youm HW, Lee JR, Lee J, Jee BC, Suh CS, Kim SH. Transplantation of mouse ovarian tissue: comparison of the transplantation sites. Theriogenology 2015;83:854–61.
[46] Kong HS, Lee J, Youm HW, Kim SK, Lee JR, Suh CS, et al. Effect of treatment with angiopoietin-2 and vascular endothelial growth factor on the quality of xenografted bovine ovarian tissue in mice. PLoS One 2017;12:e0184546.
[47] Delaglio F, Grzesiek S, Vuister GW, Zhu G, Pfeifer J, Bax Ad. NMRPipe: a multidimensional spectral processing system based on UNIX pipes. J Biomol NMR 1995;6:277–93.
[48] Goddard TD, Kneller DG. SPARKY 3. San Francisco, CA: University of California; 2003.
[49] Kneller JM, Lu M, Bracken C. An effective method for the discrimination of motional anisotropy and chemical exchange. J Am Chem Soc 2002;124:1852–3.
[50] Takamichi M, Nishimiya Y, Miura A, Tsuda S. Fully active QAE isoform confers thermal hysteresis activity on a defective SP isoform of type III antifreeze protein. FEBS J 2009;276:1471–9.
[51] Olijve LLC, Meister K, DeVries AL, Duman JG, Guo S, Bakker HJ, et al. Blocking rapid ice crystal growth through nonbasal plane adsorption of antifreeze proteins. Proc Natl Acad Sci U S A 2016;113:3740–5.
[52] Yu SO, Brown A, Middleton AJ, Tomczak MM, Walker VK, Davies PL. Ice restructuring inhibition activities in antifreeze proteins with distinct differences in thermal hysteresis. Cryobiology 2010;61:327–34.
[53] Kim HJ, Lee JH, Hur YB, Lee CW, Park SH, Koo BW. Marine Antifreeze Proteins: Structure, Function, and Application to Cryopreservation as a Potential Cryoprotectant. Mar Drugs 2017;15:27.
[54] Rubinsky B, Arav A, Fletcher GL. Hypothermic protection — a fundamental property of "Antifreeze" proteins. Biochem Biophys Res Commun 1991;180:566–71.
[55] Kobayashi J, Iwabuchi K, Miyagawa K, Sonoda E, Suzuki K, Takata M, et al. Current topics in DNA double-strand break repair. J Radiat Res 2008;49:93–103.
[56] Trapphoff T, El Hajj N, Zechner U, Haaf T, Eichenlaub-Ritter U. DNA integrity, growth pattern, spindle formation, chromosomal constitution and imprinting patterns of mouse oocytes from vitrified pre-antral follicles. Hum Reprod 2010;25:3025–42.
[57] Ball BA. Oxidative stress, osmotic stress and apoptosis: impacts on sperm function and preservation in the horse. Animal Reprod Sci 2008;107:257–67.
[58] Tatone C, Di Emidio G, Vento M, Ciriminna R, Artini PG. Cryopreservation and oxidative stress in reproductive cells. Gynecol Endocrinol 2010;26:563–7.
[59] Li Z, Lin Q, Liu R, Xiao W, Liu W. Protective effects of ascorbate and catalase on human spermatozoa during cryopreservation. J Androl 2010;31:437–44.
[60] Rahman AT, Arai T, Yamauchi A, Miura Ai, Kondo H, Ohyama Y, et al. Ice recrystallization is strongly inhibited when antifreeze proteins bind to multiple ice planes. Sci Rep 2019;9:2212.
[61] Yang DSC, Hon W-C, Bubanko S, Xue Y, Seetharaman J, Hew CL, et al. Identification of the Ice-binding surface on a type III antifreeze protein with a "flatness function" algorithm. Biophys J 1998;74:2142–51.